Journal of Physics and Chemistry of Solids 148 (2021) 109721

Contents lists available at ScienceDirect

Journal of Physics and Chemistry of Solids

journal homepage: http://www.elsevier.com/locate/jpcs

The phase multiformity and domain structure of $Sr_3Ir_2O_7$

Huaixiang Wang [a,b], Xudong Shen [a,b], Weipeng Wang [a], Yifan Ding [a,b], Yu Ji [a,b], Junkai Yang [a,b], Xi Shen [a,**], Yuan Yao [a], Youwen Long [a,b], Richeng Yu [a,b,*]

[a] Beijing National Laboratory of Condensed Matter Physics, Institute of Physics, Chinese Academy of Sciences, Beijing, 100190, PR China
[b] School of Physical Sciences, University of Chinese Academy of Sciences, Beijing, 100049, PR China

ARTICLE INFO

Keywords:
5*d*-electron TMOs
$Sr_3Ir_2O_7$
Multiformity
90° domains

ABSTRACT

Compared with 3*d*-electron transition metal oxides (TMOs), 5*d*-electron TMOs, particularly iridates, have strong competition between spin-orbit coupling and on-site Coulomb repulsion due to their comparable energies. By using aberration-corrected transmission electron microscopy, we have studied at an atomic scale the $Sr_3Ir_2O_7$ sample with a bilayered perovskite structure, which is synthesized under high pressure and high temperature. In addition, we have also investigated its magnetic and electrical properties. Our results show that the $Sr_3Ir_2O_7$ possesses two kinds of structures: a tetragonal structure (*I4/mmm*) and an orthorhombic structure (*Ccce*) with complex magnetic and electrical properties. We observed that there are often 90° domain structures along the *b* axis of the orthorhombic structure of $Sr_3Ir_2O_7$, which might be associated with the essence of antiferromagnetic 90° domains.

1. Introduction

Transition metal oxides (TMOs) have been studied for a long period due to its diverse properties, for example, high T_C superconductivity [1], magnetoresistance [2], multiferroics [3], etc. Recently, 5*d*-electron TMOs have considerably attracted much attention because of their novel electronic structures and physical phenomena [4–7]. In a conventional view, 5*d*-electron TMOs would have metal behavior due to its more extended 5*d*-electron orbit in space, which leads to wide electronic bandwidth. However, intriguing insulating behavior and anomalous magnetic characteristics were observed in some 5*d*-electron TMOs [8,9], and a peculiar effective total angular momentum $J_{eff} = 1/2$ state [4,7] caused by the comparable energy scales among crystal field splitting, on-site Coulomb repulsion U and the spin-orbit coupling (SOC) was proposed.

$Sr_3Ir_2O_7$ is one of the Ruddlesden-Popper (RP) strontium iridates $Sr_{n+1}Ir_nO_{3n+1}$ (n represents the number of Ir–O layers in a unit cell). Since the iridates have strong SOC interaction which can induce abnormal insulating states, $Sr_3Ir_2O_7$ has an anomalous magnetic state at a critical temperature with a small moment and an exotic insulating state [8]. The SOC is the relativistic effect that splits the t_{2g} band, produced by crystal field effect, into a lower $J_{eff} = 3/2$ quartet band and a higher $J_{eff} = 1/2$ doublet band [7,10], which contain four electrons and one electron, respectively. The $J_{eff} = 1/2$ band, near the Fermi level E_F, is quite narrow so that even a weak Coulomb repulsion can open a gap that induces an insulation state in $Sr_3Ir_2O_7$.

Zhang et al. [11] considered that the crystal structure of $Sr_3Ir_2O_7$ plays a crucial role in determining the physical properties. However, there is still controversy for the crystal structure of $Sr_3Ir_2O_7$. So far, three crystal structures of $Sr_3Ir_2O_7$ have been reported in the previous studies (Table 1). In Fig. 1a, we show the simulated X-ray diffraction (XRD) patterns for the three structures and find that it is quite difficult to distinguish the differences. In this work, we report the coexistence of two structures, *I4/mmm* (No.139) and *Ccce* (No.68), in polycrystalline $Sr_3Ir_2O_7$ synthesized under high pressure and high temperature. Moreover, domain structure with mutually perpendicular domains along the *b* axis occurs in the orthorhombic phase of $Sr_3Ir_2O_7$. The domain structure might induce the 90° antiferromagnetic (AFM) domain [12].

2. Experiments

Polycrystalline $Sr_3Ir_2O_7$ samples were prepared by utilizing a high-pressure approach. First, the precursors of $Sr_3Ir_2O_7$ were synthesized through the solid-state reaction. $SrCO_3$ and IrO_2 with the nominal composition of $Sr_3Ir_2O_7$ were sintered at 1173K and ambient pressure for 12 h in the air. Then, the precursors were loaded into a platinum

* Corresponding author. Beijing National Laboratory of Condensed Matter Physics, Institute of Physics, Chinese Academy of Sciences, Beijing, 100190, PR China.
** Corresponding author.
E-mail addresses: xshen@iphy.ac.cn (X. Shen), rcyu@iphy.ac.cn (R. Yu).

https://doi.org/10.1016/j.jpcs.2020.109721
Received 23 June 2020; Received in revised form 29 July 2020; Accepted 17 August 2020
Available online 26 August 2020

Table 1
Previously reported crystal structures of $Sr_3Ir_2O_7$.

Structures	Space group	Lattice Parameters	Refs.
Tetragonal	*I4/mmm*	$a \approx 3.896$ Å, $c \approx 20.879$ Å	[11–16]
Orthorhombic	*Ccce*	$a \approx 5.522$ Å, $c \approx 5.521$ Å $b \approx 20.917$ Å	[8,17,18]
Monoclinic	*C2/c*	$a \approx 20.935$ Å, $b \approx 5.518$ Å $c \approx 5.510$ Å, $\beta \approx 90.045°$	[19]

capsule and pressed up to 5 GPa using a cubic-anvil-type high-pressure apparatus at room temperature. Finally, the material was heated up to 1273K, kept for 2 h, and quenched to room temperature.

The morphology of the specimen was characterized by a scanning electron microscope (XL30 S-FEG, FEI). The phase purity of the sample was examined by a XRD equipment (Cu Kα radiation, X′ Pert Pro MPD, Philips). Magnetization and electrical resistivity as a function of temperature from 5K to 300K were measured by using a superconducting quantum interference device (SQUID) magnetometer and a physical properties measurement system (PPMS) with a standard four-probe technique, respectively.

Thin specimens for transmission electron microscopy (TEM) were prepared by milling the powders of $Sr_3Ir_2O_7$ in an agate mortar and dispersing in an amorphous carbon film supported by a copper mesh with alcohol. The selected area electron diffraction (SAED) observations were performed on a transmission electron microscope (CM200, Philips) with a field-emission gun (FEG) at 200 kV. The high-angle annular dark-field (HAADF) images were acquired on a double spherical aberration-corrected high resolution scanning transmission electron microscope (Cs-STEM, ARM200F, JEOL) with a cold FEG at 200 kV.

3. Results and discussion

Figs. 1b and c shows the schematic diagram of $Sr_3Ir_2O_7$ crystal structures, corresponding to the orthorhombic phase with *Ccce* space group and the tetragonal phase with *I4/mmm* space group, respectively. In the diagram, only a small difference between *Ccce* and *I4/mmm* phases of $Sr_3Ir_2O_7$ can be seen, which is the different situations of O atoms at Ir–O octahedra. In addition, there is a simple correlation between the two phases:

$$\boldsymbol{a}_O = \boldsymbol{a}_T + \boldsymbol{b}_T$$
$$\boldsymbol{c}_O = \boldsymbol{a}_T - \boldsymbol{b}_T$$
$$\boldsymbol{b}_O = \boldsymbol{c}_T$$

Where $\boldsymbol{a}$, $\boldsymbol{b}$ and $\boldsymbol{c}$ are the lattice unit vectors, and the subscripts "O" and "T" denote the orthorhombic and tetragonal structures, respectively. In the orthorhombic structure (*Ccce*), Ir–O octahedra are out of phase (rotate to the opposite directions along the *b* axis) in order to keep upper and lower octahedra contacted and stacking along the *b* axis. On the contrary, there is no rotation of Ir–O octahedra in the tetragonal structure (*I4/mmm*). Eight O atoms with 50% occupancy (symbolled with O') arrange in the plane rather than the four in-plane O atoms in Ir–O octahedra of the orthorhombic structure.

It's hard to define exactly the structure type from the XRD pattern as mentioned above, so we carried out TEM studies for the polycrystalline $Sr_3Ir_2O_7$. It should be noted that there are many similarities for some SAED patterns of $Sr_3Ir_2O_7$ between the tetragonal and orthorhombic phases due to the very small structural difference. The two structures have different reflection conditions. Extinction rule for tetragonal phase is: $h+k+l \neq 2n$, and for the orthorhombic phase is: $h+k \neq 2n$; $h(k) = 0$, $l \neq 2n$; h, $k \neq 2n$, $l = 0$. In Fig. 2, we present several SAED patterns that can be indexed to the tetragonal structure. Figs. 2a–d are the SAED patterns along the [001], [501], [502] and [201] zone axes, respectively. Our SAED results indicate that our polycrystalline $Sr_3Ir_2O_7$ sample contains the tetragonal phase.

Besides the tetragonal phase, we also observed a SAED pattern (Fig. 3a) that resembles Fig. 2a, except very tiny distinctions. For comparison, we present the $[001]_T$ pattern in Fig. 3c once again. Figs. 3b and d are the intensity profiles for the areas marked by dotted rectangles in Fig. 3a and c, respectively. Different from Fig. 3d, obviously, Fig. 3b has two more peaks, which means additional diffraction spots occur in Fig. 3a. Based on the detailed analysis, it was determined that Fig. 3a comes from the orthorhombic phase of $Sr_3Ir_2O_7$ and is corresponding to the $[010]_O$ zone axis. The two additional spots in Fig. 3a are the indices of $20\bar{1}$ and 201 of the orthorhombic structure. This evidence indicates that our polycrystalline $Sr_3Ir_2O_7$ sample also contains the orthorhombic phase.

Moreover, we observed another SAED pattern of the orthorhombic structure as shown in Fig. 4. In fact, Fig. 4a is a complex electron diffraction pattern which is from overlapping of the two patterns along the $[20\bar{1}]$ and [102] zone axes. In order to confirm this, we simulated electron diffraction patterns for $[20\bar{1}]$ and [102] axes and display them as well as their superimposed pattern in Fig. 4c, d and b, respectively. Fig. 4e is the magnified pattern of the red rectangle part in Fig. 4a. It is indicated that the superposition of the spots of Fig. 4c and d is just the spots arrangement case in Fig. 4a. The red and blue numbers are corresponding to the indices of the $[20\bar{1}]$ and [102] zone axes, respectively. It should also be noted that the $[20\bar{1}]$ and [102] zone axes are

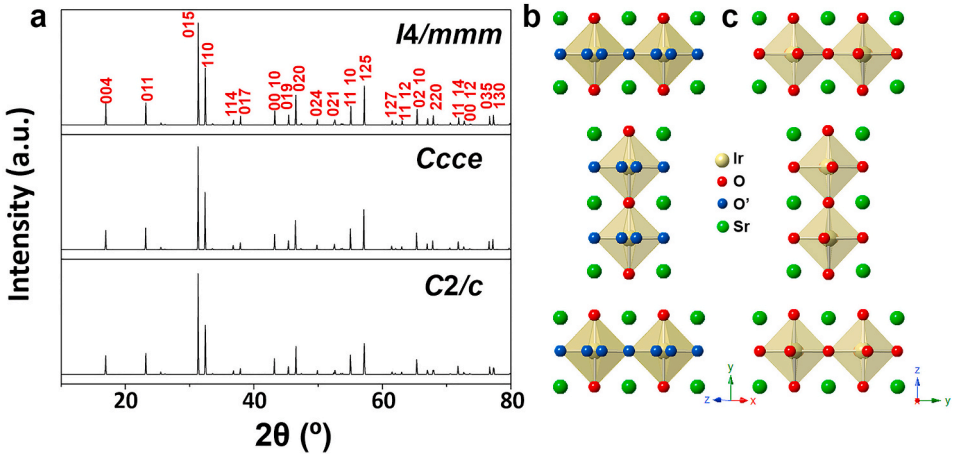

Fig. 1. (a)The simulated XRD patterns of $Sr_3Ir_2O_7$ with *I4/mmm*, *Ccce* and *C2/c* space groups, respectively ($\lambda = 1.5406$ Å). (b) The crystal structure of $Sr_3Ir_2O_7$ with *Ccce* space group. (c) The crystal structure of $Sr_3Ir_2O_7$ with *I4/mmm* space group. The yellow, red, bule and green balls represent Ir, O, O' (O atoms with 50% occupation) and Sr atoms, respectively.

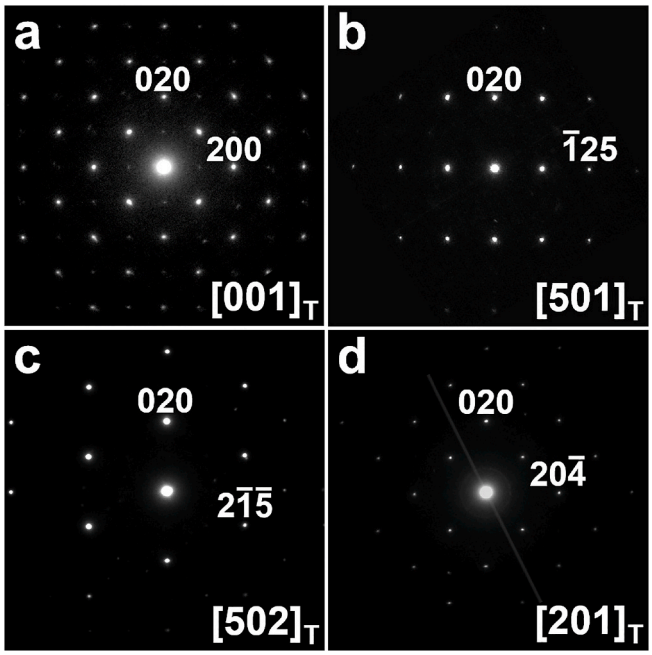

Fig. 2. The SAED patterns of polycrystalline $Sr_3Ir_2O_7$ along (a) the [001] zone axis, (b) the [501] zone axis, (c) the [502] zone axis, and (d) the [201] zone axis, respectively. The subscript 'T' indicates the tetragonal structure.

perpendicular to each other. So, Fig. 4a comes from a 90° domain structure of the orthorhombic $Sr_3Ir_2O_7$. Boseggia et al. [12] reported 90° AFM domains perpendicular to the *c* axis in the tetragonal structure (*I4/mmm*) of $Sr_3Ir_2O_7$, so it is reasonable to have 90° AFM domains in the orthorhombic $Sr_3Ir_2O_7$ correlating with the 90° structural domains.

Based on our TEM observations, we confirm that our polycrystalline $Sr_3Ir_2O_7$ contains tetragonal and orthorhombic phases. In order to determine the contents of the two components in our polycrystalline $Sr_3Ir_2O_7$ sample, we carried out Rietveld refinement for the powder XRD pattern of $Sr_3Ir_2O_7$ collected at 300K considering the coexistence of the two phases and show the results in Fig. 5. The refinement converged to $R_P = 6.66\%$ and $R_{WP} = 9.15\%$. The contents of the tetragonal and orthorhombic phases obtained from the refinement are 87.67% and 12.33%, respectively. The cell parameters and atomic coordinates are listed in Table 2. It is noted that the XRD pattern of $Sr_3Ir_2O_7$ displays almost a pure phase besides only little secondary phase of Ir as shown in Fig. 5. The inset images of Fig. 5 display scanning electron microscopy (SEM) images of the polycrystalline $Sr_3Ir_2O_7$. For the left SEM image, it is clearly seen that the polycrystalline $Sr_3Ir_2O_7$ is very dense due to the high-pressure effect during synthesis. The right SEM image is an amplified morphology that shows a grain size of ~10 μm and a rectangular and layered shape.

Fig. 6 shows scanning transmission electron microscopy (STEM) HAADF images at an atomic scale along three zone axes ($[001]_T$, $[100]_T$ and $[110]_T$) of $Sr_3Ir_2O_7$. Since the intensity is proportional to Z^2 (Z is the atomic number) [20], the brightest spots in the images represent Ir atomic columns, and the fainter spots correspond to Sr atomic columns. And the O atoms could not be observed in the HAADF image because of weak scattering. The HAADF images clearly indicate the structural characteristics of RP strontium iridates $Sr_{n+1}Ir_nO_{3n+1}$ with n = 2.

Through careful analyses of a large number of observations, we conclude that there are both tetragonal (*I4/mmm* (No.139)) and orthorhombic (*Ccce* (No.68)) phases in our polycrystalline $Sr_3Ir_2O_7$. Due to the very similar structures, we consider that the two structures may have very close ground state energies. In the synthesis of $Sr_3Ir_2O_7$, very tiny fluctuation in a local region would favor either of the two phases. Further investigation of first-principles calculations needs to be carried out. And maybe just because of the phase multiformity of $Sr_3Ir_2O_7$, diverse magnetic properties were observed in the previous works [8,12,16,21].

Magnetizations as a function of temperature obtained in a zero field cooling (ZFC) and a field cooling (FC) for $Sr_3Ir_2O_7$ are shown in Fig. 7a, respectively. The ZFC curve was measured during a heating procedure at an excitation field $H = 100$Oe after cooling to 5K from room temperature and the FC data were obtained from another heating procedure at the same field $H = 100$Oe after cooling at $H = 100$Oe from room temperature. Fig. 7b shows the derivative ($\partial M/\partial T$) of FC data, from which three transitions at $T_X = 202$K, $T_B = 235$K and $T_N = 284$K are presented. It should be noted that T_X and T_B are the same in both ZFC and FC procedures, while the transition at T_N, which is consistent with the earlier studies [8], is only detected in FC procedure. Moreover, a noticeable downturn below 100 K [8,12,21] in FC procedure is not observed for our sample.

Here, T_N is regarded as a collinear AFM transition temperature, which comes from the strong coupling of bilayer antiferromagnet [18,21], and the transition at T_B is consider to originate from a

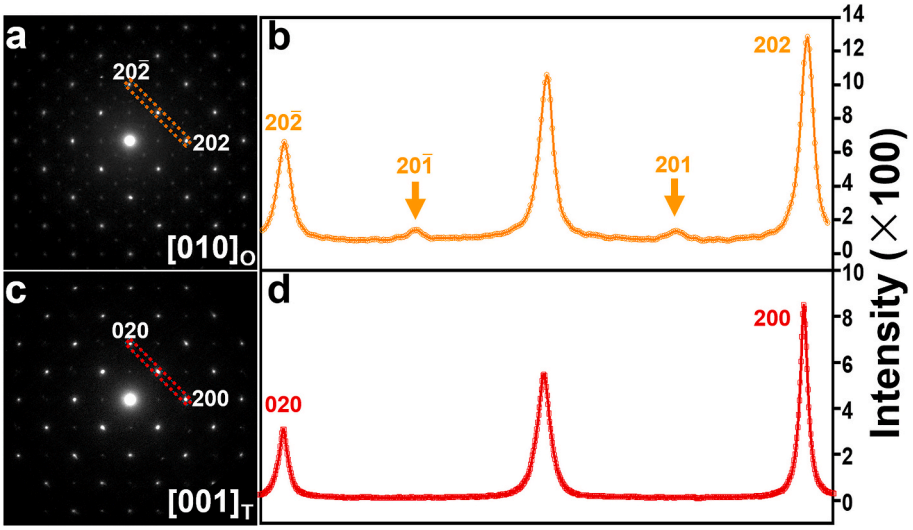

Fig. 3. (a) The SAED pattern of $Sr_3Ir_2O_7$ along [010] zone axis of the orthorhombic structure. (b)The intensity profile for the marked area in (a). (c) The SAED pattern of $Sr_3Ir_2O_7$ along [001] zone axis of the tetragonal structure. (d) The intensity profile for the marked area in (c). The subscripts 'T' and 'O' indicate the tetragonal and orthorhombic structures, respectively.

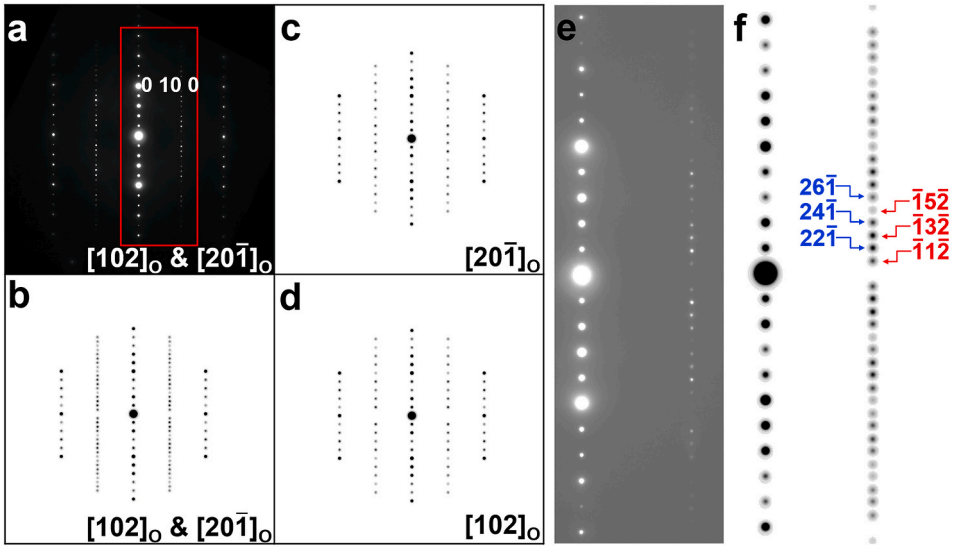

Fig. 4. The SAED patterns of the orthorhombic structure of $Sr_3Ir_2O_7$. (a) The superimposed pattern along the [102] and [20$\bar{1}$] zone axes. (b)The superimposed pattern of (c) and (d). (c) and (d) Simulated SAED patterns along the [20$\bar{1}$] and [102] zone axes, respectively. (e) The magnified pattern of the red rectangle part in (b). (f) Simulated superimposed SAED pattern along the [102] and [20$\bar{1}$] zone axes. The red and blue numbers are corresponding to the indices in (c) and (d), respectively.

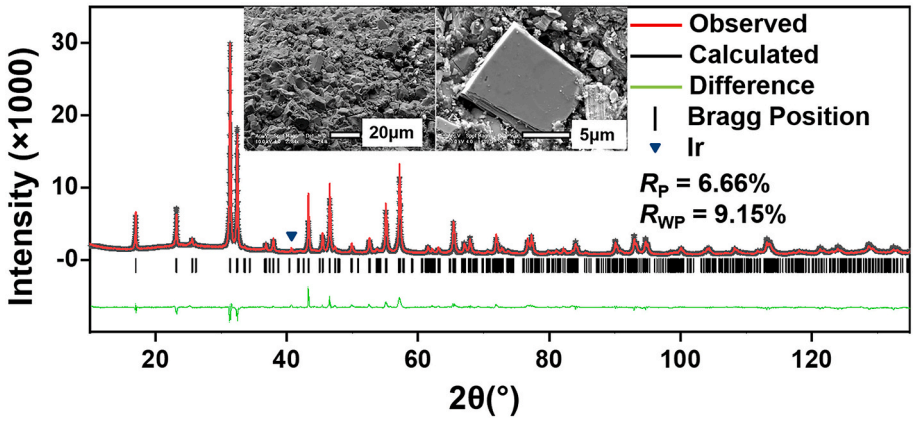

Fig. 5. Retiveld refinement of powder X-ray diffraction pattern of $Sr_3Ir_2O_7$. The blue triangle indicates the Ir phase. Inset: The SEM images of the polycrystalline $Sr_3Ir_2O_7$.

Table 2
Cell parameters and atomic coordinates of $Sr_3Ir_2O_7$.

Space group	*I4/mmm*				*Ccce*			
Cell parameters(Å)	$a = b = 3.9015$, $c = 20.8980$			Site Occ.	$a = 5.5309$, $b = 20.9003$, $c = 5.5182$			Site Occ.
Atom	x	y	z	1	x	y	z	1
Ir	0	0	0.0979	1	0	0.1523	0.25	1
O1	0	0.3982	0.4091	0.5	0	0.25	0.25	1
O2	0	0	0.2030	1	0	0.0419	0.25	1
O3	0	0	0	1	0.0887	0.1707	0.8287	1
Sr1	0	0	0.3122	1	0	0.25	0.75	1
Sr2	0	0	0.5	1	0	0.5882	0.25	1

magnetostrictive distortion [8]. However, our T_N (similar transition denoted by T_A, T_N and T_{AF} in Refs. [8,16,21], respectively) and T_B (similar transition represented by T_B, T^* and T_O in Refs. [8,16,21], respectively) values are different from the earlier studies, where the transition temperature values are also inconsistent in each report, T_B = 260K and T_A (T_N) = 285K in Ref. 8, T_B = 230K and T_A (T_N) = 275K in Ref. 12, T^* (T_B) = 240K and T_N = 290K in Ref. 16, and T_O (T_B) = 220K and T_{AF} (T_N) = 280K in Ref. 21. Besides T_B = 235K and T_N = 284K, we also observed an additional transition at T_X. It should be noted that Ir is paramagnetic [22]. Due to the coexistence of the tetragonal and orthorhombic structures in our sample, we consider that T_X and T_B might be caused by the corresponding magnetostrictive distortion of the two phases. Further investigations are undergoing. Interestingly, the transitions are observed in ZFC procedure for our sample, which were not

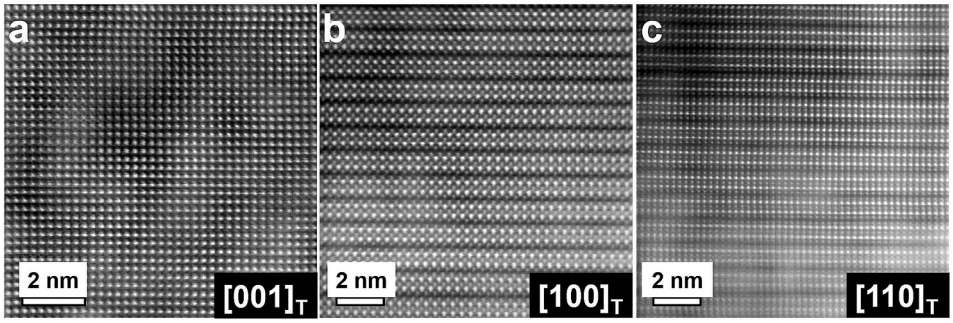

Fig. 6. (a, b and c) The HAADF images of $Sr_3Ir_2O_7$. Along the [001], [100] and [110] axes, respectively. The subscript "T" represents the tetragonal structure.

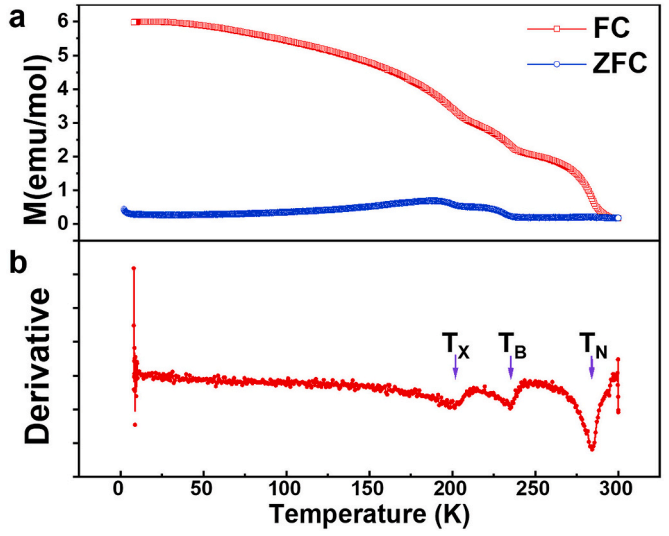

Fig. 7. (a) ZFC (open blue circle) and FC (open red square) curves of $Sr_3Ir_2O_7$ measured at $H = 100$Oe from 5K to 300K. (b) The derivative ($\partial M/\partial t$) of FC data. The purple arrows at $T_X = 202$K, $T_B = 235$K and $T_N = 284$K indicate transitions in FC curve.

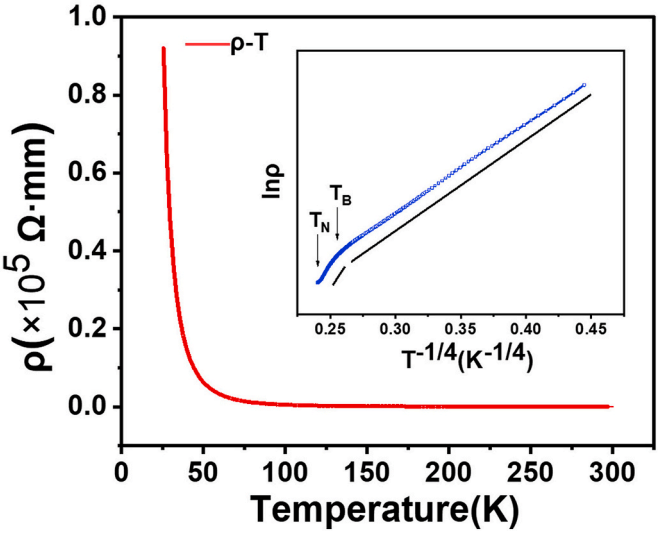

Fig. 8. Resistivity versus temperature for $Sr_3Ir_2O_7$. Inset: lnρ versus $T^{-1/4}$ curve. $T_B = 235$K and $T_N = 284$K marked by arrows are consistent with that in Fig. 8.

detected in previous reports. Different magnetism behavior of our sample maybe originates from different synthesis routes. This may be the reason why different transition temperature values of $Sr_3Ir_2O_7$ in FC procedure were reported [8,12,16,21].

Fig. 8 is the electrical resistivity of polycrystalline $Sr_3Ir_2O_7$ as a function of temperature. It obviously shows insulating behavior. We fit the data in the range of 5K to room temperature with a variable range hopping (VHR) model which explains the conductive mechanism in materials and obeys the formula $\rho = \rho_0 \exp(T_M/T)^{1/(D+1)}$, where T_M and ρ_0 are constants, D is the dimensionality of the system. The inset in Fig. 8 represents lnρ versus $T^{-1/4}$, which signifies a 3D VRH for the $Sr_3Ir_2O_7$. Moreover, it clearly indicates two transition temperatures at $T_B = 235$K and $T_N = 284$K, consistent with the result from M-T curves. Though the lnρ versus $T^{-1/4}$ curve can be expressed by a 3D VRH, the fitted curve shows two linear regions with different slopes (below T_B and $T_B \sim T_N$), which indicate different density of states and localized ranges of electrons in the two temperature ranges [23,24].

4. Conclusions

We confirm that two phases, the tetragonal and orthorhombic phases, coexist in the high pressure synthesized polycrystalline $Sr_3Ir_2O_7$ sample. Especially, 90° structural domains in the orthorhombic phase are observed, which may be accompanied with the antiferromagnetic domains. The measurements of magnetic and transport properties both show the consistent transition temperatures, indicating complex, intrinsic and intriguing physical connotations of $Sr_3Ir_2O_7$.

Credit author statement

Huaixiang Wang: Performed the experiments and acquired data, Data curation, Analyzed and interpreted the data, Formal analysis, Drafted the manuscript, Writing - original draft, Carried out the simulations. **Xudong Shen:** Performed the experiments and acquired data, Data curation. **Weipeng Wang:** Performed the experiments and acquired data, Data curation. **Yifan Ding:** Carried out the simulations. **Yu Ji:** Performed the experiments and acquired data, Data curation. **Junkai Yang:** Carried out the simulations. **Xi Shen:** Analyzed and interpreted the data, Formal analysis, Conceived and designed the study. **Yuan Yao:** Analyzed and interpreted the data, Formal analysis. **Youwen Long:** Analyzed and interpreted the data, Formal analysis. **Richeng Yu:** Conceived and designed the study, Analyzed and interpreted the data, Formal analysis.

Declaration of competing interest

Here we claim that we have no conflict of interest for this paper.

Acknowledgements

This work was supported by the National Key Research Program of China (Grant Nos. 2017YFA0206200, 2016YFA0300701 and 2018YFA0208402), the National Natural Science Foundation of China

(Grant Nos. 11874413, 11934017, 11574376 and 51972333) and the Strategic Priority Research Program of the Chinese Academy of Sciences, No. XDB33030200. One of the authors, X. Shen, was sponsored by the Youth Innovation Promotion Association of CAS (2019009).

Appendix A. Supplementary data

Supplementary data related to this article can be found at https://doi.org/10.1016/j.jpcs.2020.109721.

References

[1] H. Yang, Q.Q. Liu, R.C. Yu, F.Y. Li, C.Q. Jin, Supercond. Sci. Technol. 18 (2005) 813.
[2] L.D. Yao, W. Zhang, J.S. Zhang, H. Yang, F.Y. Li, Z.X. Liu, C.Q. Jin, R.C. Yu, J. Appl. Phys. 101 (2007), 063905.
[3] Q.H. Zhang, G.T. Tan, L. Gu, Y. Yao, C.Q. Jin, Y.G. Wang, X.F. Duan, R.C. Yu, Sci. Rep. 3 (2013) 2741.
[4] B.J. Kim, H. Ohsumi, T. Komesu, S. Sakai, T. Morita, H. Takagi, T. Arima, Science 323 (2009) 1329.
[5] Y. Okada, D. Walkup, H. Lin, C. Dhital, T.-R. Chang, S. Khadka, W. Zhou, H.-T. Jeng, M. Paranjape, A. Bansil, Z. Wang, S.D. Wilson, V. Madhavan, Nat. Mater. 12 (2013) 707.
[6] H. Chu, L. Zhao, A. de la Torre, T. Hogan, S.D. Wilson, D. Hsieh, Nat. Mater. 16 (2017) 200.
[7] B.J. Kim, H. Jin, S.J. Moon, J.-Y. Kim, B.-G. Park, C.S. Leem, J. Yu, T.W. Noh, C. Kim, S.-J. Oh, J.-H. Park, V. Durairaj, G. Cao, E. Rotenberg, Phys. Rev. Lett. 101 (2008), 076402.
[8] G. Cao, Y. Xin, C.S. Alexander, J.E. Crow, P. Schlottmann, M.K. Crawford, R. L. Harlow, W. Marshall, Phys. Rev. B 66 (2002) 214412.
[9] G. Cao, J. Bolivar, S. McCall, J.E. Crow, R.P. Guertin, Phys. Rev. B 57 (1998) R11039.
[10] S.J. Moon, H. Jin, K.W. Kim, W.S. Choi, Y.S. Lee, J. Yu, G. Cao, A. Sumi, H. Funakubo, C. Bernhard, T.W. Noh, Phys. Rev. Lett. 101 (2008) 226402.
[11] J. Zhang, D. Yan, S. Yesudhas, H. Deng, H. Xiao, B. Chen, R. Sereika, X. Yin, C. Yi, Y. Shi, Z. Liu, E.M. Pärschke, C.-C. Chen, J. Chang, Y. Ding, H. Mao, Npj Quantum Mater 4 (2019) 23.
[12] S. Boseggia, R. Springell, H.C. Walker, A.T. Boothroyd, D. Prabhakaran, D. Wermeille, L. Bouchenoire, S.P. Collins, D.F. McMorrow, Phys. Rev. B 85 (2012) 184432.
[13] M.A. SubramAnlan, M.K. Crawford, R.L. Harlow, Mater. Res. Bull. 29 (1994) 645.
[14] J.A. Kafalas, J.M. Longot, J. Solid State Chem. 4 (1972) 55.
[15] I. Nagai, Y. Yoshida, S.I. Ikeda, H. Matsuhata, H. Kito, M. Kosaka, J. Phys. Condens. Matter 19 (2007) 136214.
[16] I. Pallecchi, M.T. Buscaglia, V. Buscaglia, E. Gilioli, G. Lamura, F. Telesio, M. R. Cimberle, D. Marré, J. Phys. Condens. Matter 28 (2016), 065601.
[17] H. Matsuhata, I. Nagai, Y. Yoshida, S. Hara, S. Ikeda, N. Shirakawa, J. Solid State Chem. 177 (2004) 3776.
[18] S. Fujiyama, K. Ohashi, H. Ohsumi, K. Sugimoto, T. Takayama, T. Komesu, M. Takata, T. Arima, H. Takagi, Phys. Rev. B 86 (2012) 174414.
[19] T. Hogan, L. Bjaalie, L. Zhao, C. Belvin, X. Wang, C.G. Van de Walle, D. Hsieh, S. D. Wilson, Phys. Rev. B 93 (2016) 134110.
[20] S.J. Pennycook, L.A. Boatner, Nature 336 (1988) 565.
[21] C. Dhital, S. Khadka, Z. Yamani, C. de la Cruz, T.C. Hogan, S.M. Disseler, M. Pokharel, K.C. Lukas, W. Tian, C.P. Opeil, Z. Wang, S.D. Wilson, Phys. Rev. B 86 (2012) 100401.
[22] R. David Lide, Handb. Chem. Phys. 81 (2005).
[23] N. Francis Mott, Philos. Magazine. Informa UK Limited. 19 (1969) 835.
[24] N. Apsley, H.P. Hughes, Philos. Magazine. Informa UK Limited. 30 (1974) 963.